Identification of crystalline elastic anisotropy in PZT ceramics from *in-situ* blocking stress measurements

L. Daniel,[1,2,a)] D. A. Hall,[1] K. G. Webber,[3] A. King,[4,5] and P. J. Withers[1]
[1]*School of Materials, University of Manchester, Manchester M13 9PL, United Kingdom*
[2]*LGEP (CNRS UMR8507, SUPELEC, UPMC, Univ Paris-Sud), 91192 Gif sur Yvette cedex, France*
[3]*Institute of Materials Science, Technische Universität Darmstadt, Alarich-Weiss-Straße 2, 64287 Darmstadt, Germany*
[4]*European Synchrotron Radiation Facility (ESRF), 6 rue J. Horowitz, 38043 Grenoble, France*
[5]*Synchrotron SOLEIL, BP 48, 91192 Gif sur Yvette cedex, France*

(Received 31 January 2014; accepted 19 April 2014; published online 2 May 2014)

High energy x-ray diffraction measurements of lattice strains were performed on a rhombohedral Lead Zirconate Titanate ceramic (PZT 55-45) under combinations of applied electric field and compressive stress. These measurements allow the construction of blocking stress curves for different sets of crystallographic orientations which reflect the single crystal elastic anisotropy. A micro-mechanical interpretation of the results is then proposed. Assuming cubic symmetry for the crystalline elastic stiffness tensor and isotropy for the macroscopic elastic properties, the elastic properties of the single crystal are extracted from the measured data. An anisotropy ratio close to 0.3 is found (compared to 1 for isotropic materials). The high level of anisotropy found in this work suggests that crystalline elastic anisotropy should not be neglected in the modelling of ferroelectric materials. [http://dx.doi.org/10.1063/1.4874222]

I. INTRODUCTION

Piezoelectric ceramics are widely used as the basis for electromechanical sensors and actuators for control, medical, electronic, and micro-electromechanical systems (MEMS) applications. Electromechanical actuators exploit the electric field-induced strain, which can be represented by the linear converse piezoelectric effect.[1] In many applications, piezoelectric ceramic materials are subject to relatively high levels of applied electric field and/or mechanical stress, which introduce significant nonlinearity into the dielectric, elastic, and piezoelectric relationships; this nonlinearity arises as a result of ferroelectric and ferroelastic domain switching.[1–4]

The macroscopic strain under a given set of external loading conditions can be understood as being due to a complex combination of the intrinsic piezoelectric effect, the extrinsic effects resulting from non-180° domain switching, and the development of internal inter-granular stresses. Depending on the composition, some materials can also undergo phase switching.[5,6] With such complex mechanisms underlying their macroscopic behaviour, ferroelectric materials can neither be described using simple models nor can they be fully understood on the basis of macroscopic measurements alone.

In recent years, diffraction techniques have been exploited as a means of evaluating the local lattice strain and domain switching behaviour of polycrystalline ferroelectric materials in response to external electric and/or mechanical loading.[7–16] For example, Hall *et al.* demonstrated that poling ferroelectric ceramics induces a remanent lattice strain along certain crystallographic directions, which is caused by residual stresses associated with ferroelectric domain switching.[7–9] Pramanick *et al.* determined the lattice strains and domain switching behaviour in PZT (lead zirconate titanate) ceramics by conducting *in-situ* diffraction experiments in the sub-coercive field region;[13,14] these authors quantified the intrinsic and extrinsic contributions to the total strain, including both linear and nonlinear terms. It was shown that inter-granular interactions (i.e., residual stress) in polycrystalline ferroelectrics can account for a significant proportion of the macroscopic electromechanical response, which distinguishes their behaviour from that of single crystals. Diffraction methods have also been used to identify novel mechanisms for electromechanical actuation in certain lead-free piezoelectric ceramics.[15,16]

Piezoelectric devices are frequently used under combined electrical and mechanical loading, for example, in high power acoustic transducers and multilayer stack actuators. For the case of actuators, the performance of a device in the presence of a restraining force or static stress can be characterised by measuring the so-called blocking stress relationship.[17] This is achieved by recording the stress-strain relationships under a given set of static electric field levels. The blocking stress is, for a given intensity of electric field, the amplitude of the compressive stress required to cancel the piezoelectric strain. Although it is known that non-180° domain switching plays an important role in determining the electro-mechanical behaviour of actuator materials under stress,[18] there are currently no reports of *in-situ* measurements of blocking stress curves by diffraction methods.

The present paper presents the results of an *in-situ* synchrotron x-ray diffraction (XRD) study on a rhombohedral PZT 55-45 ceramic under combined electrical and mechanical loading. Although much research has been conducted to

a)Author to whom correspondence should be addressed. Electronic mail: laurent.daniel@u-psud.fr

find alternative lead-free compositions, PZT ceramics still represent the dominant type of piezoceramic in commercial applications. It is shown that in the case of the material studied, little domain switching occurs under moderate stress at constant electric field. This particular observation allows the identification of the single crystal anisotropy using simple homogenisation modelling techniques (micro-mechanical effective medium approaches). The anisotropy ratio obtained suggests a significant role of local elastic anisotropy in the development of internal stresses under electro-mechanical loading.

II. MATERIAL PREPARATION AND EXPERIMENTS

A. Material preparation and macroscopic properties

In this study, the *in-situ* constitutive behaviour of $Pb_{0.98}Ba_{0.01}(Zr_{0.55}Ti_{0.45})_{0.98}Nb_{0.02}O_3$ (PZT 55-45) was characterised during electromechanical loading. The powders were prepared with the mixed-oxide method using PbO (Sigma, 99.9% purity), TiO_2 (Alfa, 99.8% purity), ZrO_2 (TZ-0, Tosoh), Nb_2O_5 (Sigma, 99.9% purity), and $BaCO_3$ (Alfa, 99.8% purity) as precursors. Prior to sintering, the powder mixtures were homogenised in isopropyl alcohol (C_3H_7OH) in a planetary mill, followed by two calcinations at 900 °C for 1 h (heating/cooling rate of 5 °C/min). The powder was milled after each calcination step. The resultant powder mixture was dried, sieved, and pressed into pellets and sintered at 1275 °C for 2 h with a heating/cooling rate of 5 °C/min. The mean Ferets diameter of the grain size ($d_F \pm$ std. dev.) and theoretical density, determined by the Archimedes method, were found to be $4.0 \pm 1.9\,\mu$m and 97.1%, respectively. The processing details have been previously described elsewhere.[19] Previous XRD investigations have revealed that PZT 55-45 is rhombohedral with a minority tetragonal phase,[19] showing the close proximity of this composition to the morphotropic phase boundary (MPB). The sintered material was then sectioned and ground into bars having a final geometry of $1\,\text{mm} \times 1\,\text{mm} \times 3\,\text{mm}$ for synchrotron measurements. Silver electrodes were sputtered onto opposing $1\,\text{mm} \times 3\,\text{mm}$ faces for the application of electrical fields.

The macroscopic electrical and mechanical constitutive behaviour was characterised at room temperature for PZT 55-45. Before testing, the samples were thermally depoled to ensure a virgin state. During electrical testing, a triangular wave with a maximum electric field of 5 kV/mm and a frequency of 50 mHz was applied to circular samples (4 mm diameter, 1 mm thick). PZT 55-45 was found to display a coercive field of approximately 0.85 kV/mm as well as a remanent strain and polarisation of 0.35% and 42 μC/cm^2, respectively (Fig. 1). The maximum strain at 5 kV/mm was 0.57%, and the observed large field piezoelectric coefficient ($\tilde{d}_{33}$) was 440 pm/V.

Samples for mechanical testing were approximately 6 mm in height and 5.8 mm in diameter. Prior to testing, the samples were electrically poled at 120 °C at 2 kV/mm for 5 min, followed by cooling to room temperature with the field still applied. After the poling process, samples were short-circuited and a maximum compressive stress of 500 MPa was applied with a loading/unloading rate of 4 MPa/s at room temperature, during which the strain and polarisation were recorded (Fig. 2). From the mechanical tests, PZT 55-45 was found to have a coercive stress of approximately -45 MPa as well as a remanent strain and remanent polarisation of 0.64% and 41 μC/cm^2, respectively. The coercive stress corresponds well to previous investigations.[19,20] The mechanically induced decrease in polarisation closely corresponds to the observed remanent polarisation during electrical loading. In addition, previous investigations on the mechanical properties of PZT 55-45 have shown the remanent strain of unpoled samples after mechanical compression to be 0.30%,[19,20] which when combined with the electrically induced remanent strain (0.35%) during poling (Fig. 1(b)) shows excellent agreement with the observed remanent strain during mechanical loading of poled samples (0.64%).

B. Diffraction experiments

The x-ray diffraction experiments were performed at the ID11 beamline at the European Synchrotron Radiation Facility (ESRF, Grenoble, France). This is a beamline for materials science and crystallography, optimised for high beam energies, and with flexible beam optics.[21] For these measurements, the x-ray photon energy was calibrated by scanning across the Pt absorption edge at 78.395 keV and then set to this energy. Two in-vacuum undulators provide

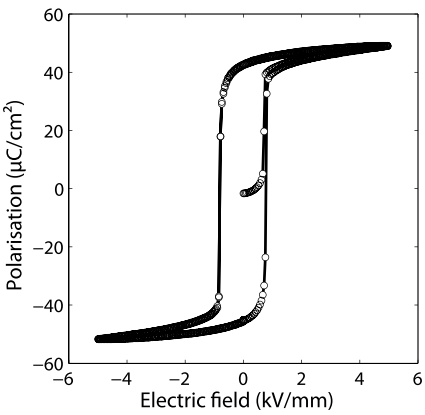

(a) Macroscopic Polarisation-electric field loop

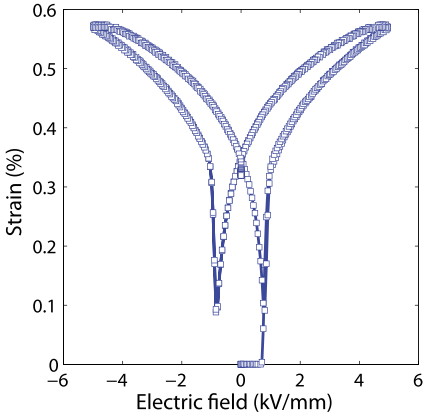

(b) Macroscopic strain-electric field loop

FIG. 1. Macroscopic behaviour of PZT 55-45 at room temperature.

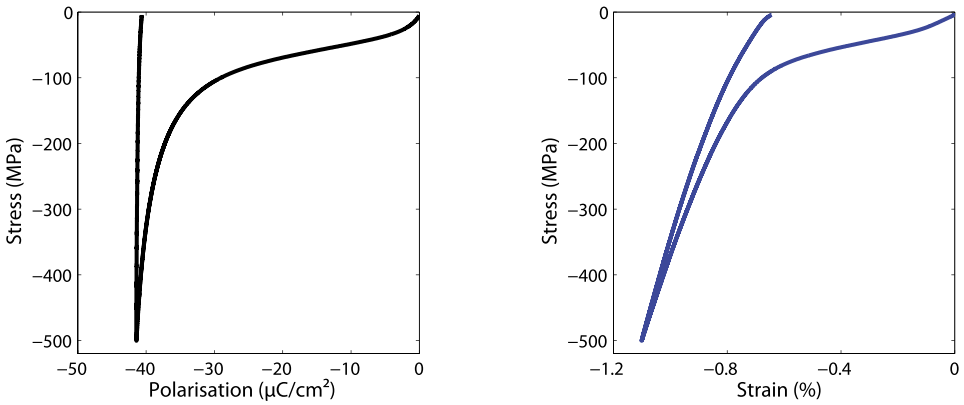

(a) Stress-polarisation curves (b) Stress-strain curves

FIG. 2. Macroscopic behaviour of PZT 55-45 under compressive loading-unloading at room temperature.

an intense beam of x-rays. Due to the high x-ray energy, the wavelength ($\lambda = 0.1515 \times 10^{-10}$ m), and the scattering angle 2θ (less than 5°) are both small. The measured lattice planes are then almost perpendicular to the vertical axis **z** for $\psi = 0°$ and to the horizontal axis **y** for $\psi = 90°$. The direction normal to the diffracting planes is approximately in the **y**-**z** plane perpendicular to the beam direction **x**.

Diffraction patterns were recorded using an ESRF FReLoN CCD camera, coupled to a visible light scintillator via a fibre optic taper.[22,23] This provides an effective pixel size of around 50 μm, and a field of view of 100×100 mm^2. Acquisition time was set to 10 s per image. To improve angular resolution and resolve overlapping diffraction peaks, the beam was collimated using compound refractive lenses in the in-vacuum transfocator and slits used to define a beam-size of $100 \times 100\,\mu$m^2 at the sample position. For the same reason, the distance between sample and detector was increased to 1 m from the sample and offsets horizontally and vertically in order to record only a quadrant of the Debye-Scherrer rings, as shown in Fig. 3. The detector position was calibrated by recording diffraction patterns from a standard Ceria powder. The standard was mounted to the side of the stress rig so that calibration patterns could be recorded systematically during the experiment.

The experimental rig (Fig. 4) comprises two metallic pieces between which the specimen is placed. A steel ball is used as a ball-and-socket joint to ensure a solely uniaxial compression state in the specimen. The specimen itself is surrounded by oil (Fluorinert™ FC-70 Electronic Liquid) to prevent arcing during the application of the electric field. An electric field up to 4 kV/mm was applied using a high voltage amplifier (Chevin Research HVA1B). The whole rig was mounted in a compact MTEST Quattro Materials Testing System loading device[24] to apply the stress.

The experimental procedure was as follows: the sample was first poled, or repoled, under an electric field of 4 kV/mm. From this poled state, a static electric field E was applied, modifying the strain of the material through the piezoelectric effect. This change in strain was monitored by measuring the {200} peak position. Potential domain switching was monitored by measuring the {111} peaks positions and intensities. A compressive stress was then applied to the material, so as to approximately cancel the piezoelectric strain. During this process, the lattice spacing d_{hkl} of selected planes was measured *in-situ*. Both single and double peak profiles have been fitted using a Matlab procedure based on pseudo-Voigt distribution functions. Upon releasing the stress, a new cycle was initiated for another

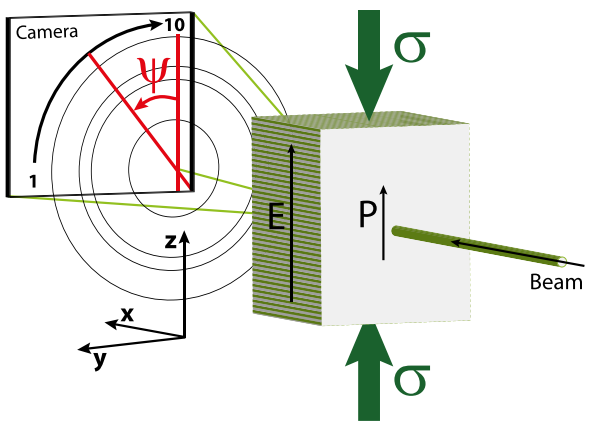

FIG. 3. Schematic view of the measurement configuration. Electric field and stress are parallel. The incident beam is normal to the electric field. The camera is placed so as to capture a quadrant of the rings in order to increase resolution. The results are divided into ten banks denoted 1 to 10, corresponding to an azimuthal angle ψ from 90° to 0°.

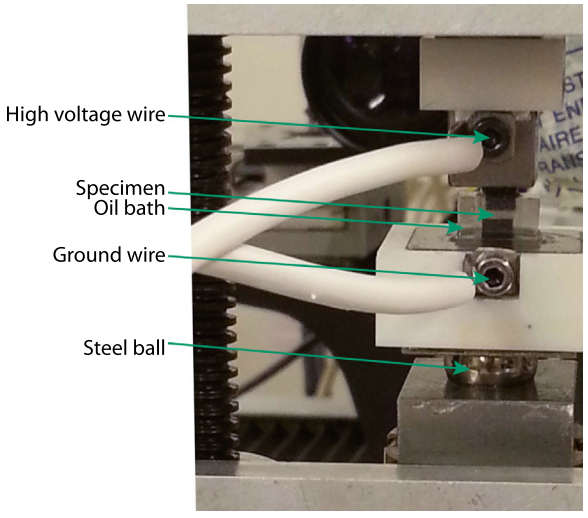

FIG. 4. Photo of the measurement rig mounted in the electromechanical compression device.

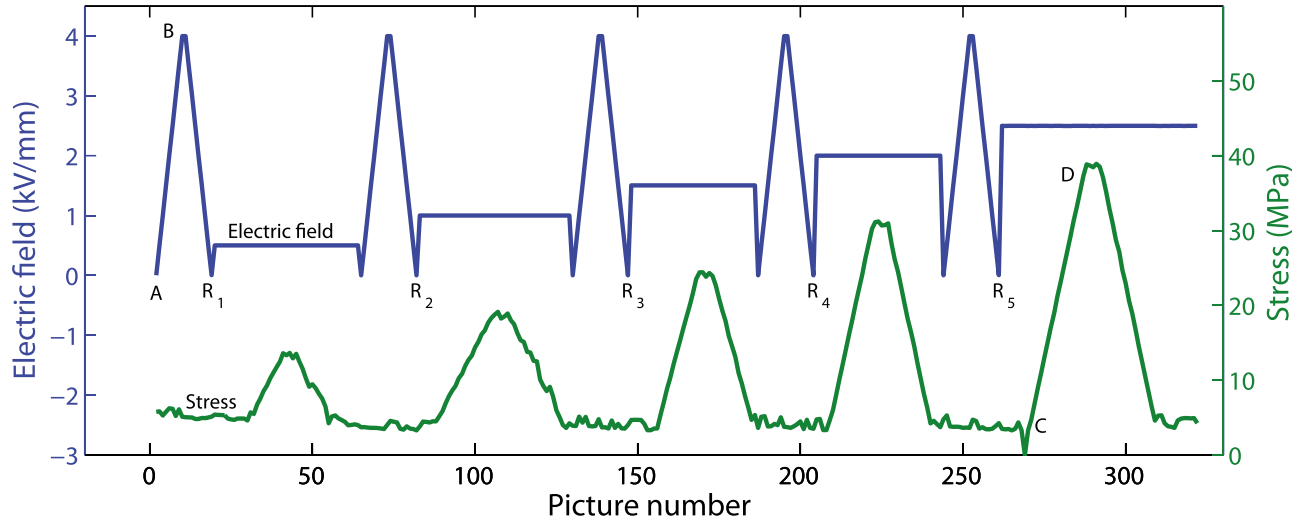

FIG. 5. External electro-mechanical loading during the *in-situ* experiment: electric field (top) and compressive stress (bottom).

value of the electric field E. The loading sequence is presented in Fig. 5. In order to maintain contact between the mechanical loading frame and the testing rig, a minimum compressive stress of approximately 5 MPa was maintained during the whole procedure. The reference state for the experiment is taken to be the state just after poling (points R_1 to R_5 in Fig. 5). It was found that this reference state was relatively stable during the experiment, since similar diffraction patterns were obtained after each repoling procedure.

III. RESULTS

Selected regions of the diffraction patterns obtained during the experiment are presented in Figs. 6 and 7. The single {200} peak and split {111} peaks are typical for a rhombohedrally distorted perovskite ferroelectric.[9] From the difference in position between (111) and ($\bar{1}$11) peaks, domain switching can be estimated to generate a maximum strain of approximately 0.7% along ⟨111⟩ directions. Previous laboratory diffraction measurements on the same material[19,20] reported a slight distortion of the diffraction profile attributed to the presence of a minority tetragonal phase. This distortion has not been observed here. This could be due to the difference in resolution between synchrotron and laboratory XRD apparatus or to a slight difference in composition between the bulk (sampled by synchrotron x-rays) and the surface (sampled by laboratory x-rays) for this material. The relative heights of the {111} peaks indicate that the specimen was already in a well-

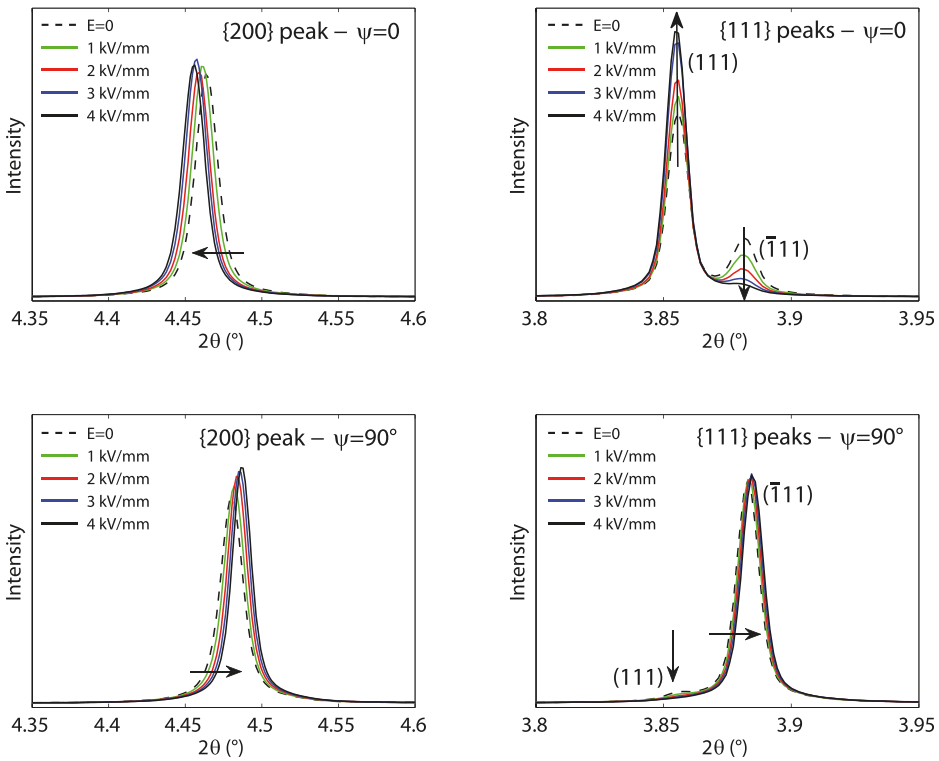

FIG. 6. Diffraction patterns for the first electric field loading (points A to B in Fig. 5): {111} and {200} peaks for $\psi = 0°$ and $\psi = 90°$. The dominance of the (111) peak for $\psi = 0$ and the ($\bar{1}$11) peak for $\psi = 90°$ confirm that the material is initially in a well-poled state. The profiles are given for E = 0, 1, 2, 3, and 4 kV/mm.

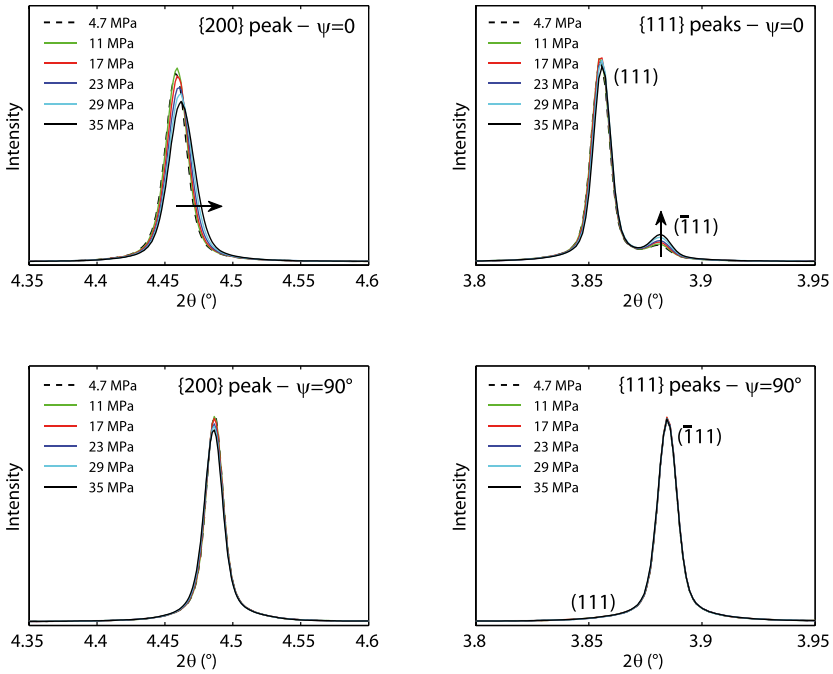

FIG. 7. Diffraction patterns for the last stress loading (points C to D in Fig. 5): {111} and {200} peaks for $\psi = 0°$ and $\psi = 90°$. The patterns show very little domain switching under stress. The profiles are given for $\sigma = 4.7$, 11, 17, 23, 29, and 35 MPa.

poled state at the start of the experiment, with the (111) peak being dominant for $\psi = 0°$ and the $(\bar{1}11)$ peak for $\psi = 90°$. The position of the {200} peak was also dependent on the grain orientation, indicating the occurrence of a tensile intergranular residual stress for $\psi = 0°$ and a compressive intergranular residual stress for $\psi = 90°$. These observations are consistent with those reported in the previous publications.[7,9]

For $\psi = 0°$, increasing electric field strength caused a further shift of the {200} peak to smaller 2θ values, caused by an increasing tensile lattice strain, while the (111) peak intensity was significantly enhanced relative to that of the $(\bar{1}11)$ peak due to ferroelectric domain switching towards the poling direction (Fig. 6). The opposite trends were observed for $\psi = 90°$, indicating the development of a compressive strain and ferroelectric domain switching away from the transverse directions.

In contrast, the application of a uniaxial compressive stress along the macroscopic polar axis led to a shift of the (200) peak to higher 2θ values caused by compressive strain for $\psi = 0°$ (Fig. 7). In this case, there was only a slight change in the relative intensities of the (111) and $(\bar{1}11)$ peaks, suggesting that there was a relatively small amount of ferroelastic domain switching for applied stresses in the range 5 to 35 MPa, particularly when a static electric field was also present.

The evolution of the {200} and {111} lattice spacings during the course of the experiment is presented in Figs. 8 and 9, respectively. Here, d_{200} is simply the inter-planar spacing for the {200} planes, while d_{111} is the weighted average of the lattice spacings for the (111) and $(\bar{1}11)$ peaks; therefore, it should be noted that d_{111} incorporates a dependence on the degree of ferroelectric domain switching in addition to the true lattice strain. The changes in d_{200} as a function of the frame number, presented in Fig. 8, correlate well with the variations in applied electric field and compressive stress, plotted in Fig. 5. For $\psi = 0°$, the initial positive excursion between frames 0 and 30

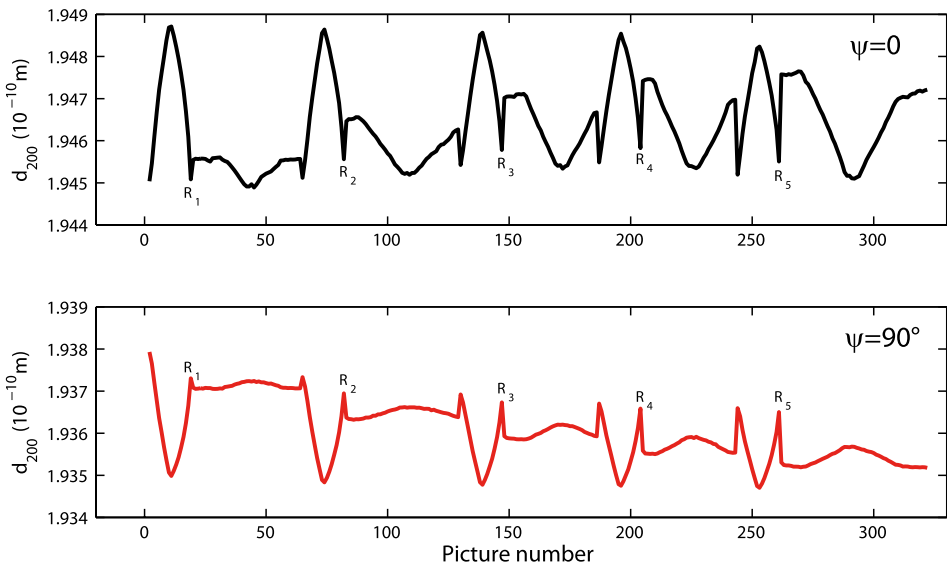

FIG. 8. Evolution of d_{200} during the *in-situ* experiment, $\psi = 0°$ (top) and $\psi = 90°$ (bottom).

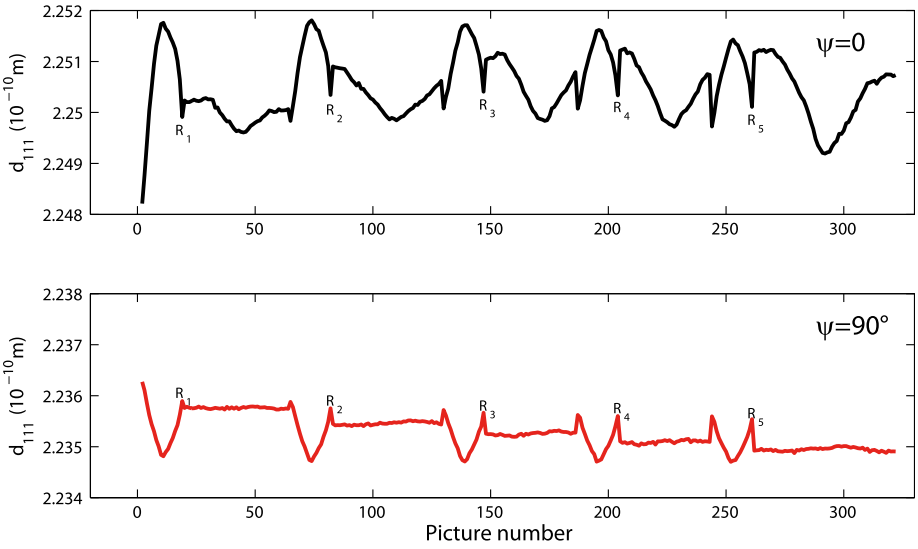

FIG. 9. Evolution of d_{111} during the *in-situ* experiment, $\psi = 0°$ (top) and $\psi = 90°$ (bottom).

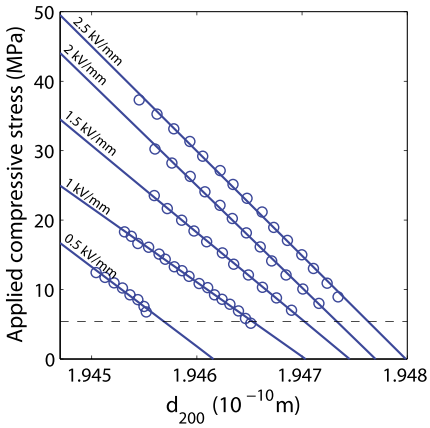

(a) {200} blocking stress curves.

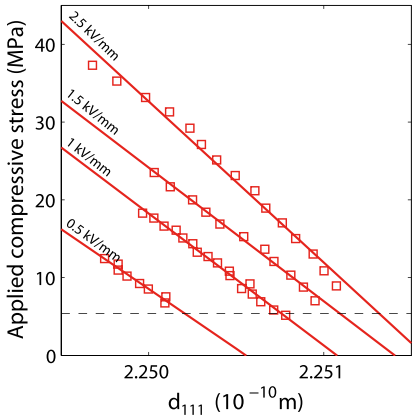

(b) {111} blocking stress curves.

FIG. 10. Analysis of diffraction profiles: blocking stress curves obtained for $\psi = 0°$ at several levels of applied electric field. Experimental measurements (markers) and corresponding linear fitting (lines). The horizontal dashed line shows the prestress level to maintain contact between the mechanical loading frame and the testing rig.

corresponds to the first electrical poling procedure, while the subsequent negative excursion between frames 20 and 60 corresponds to the application of the first compressive stress cycle. As the experiment progressed, the starting point for each stress cycle gradually shifted upwards as a result of the increasing static electric field and the negative excursions grew in magnitude due to the gradual application of higher ultimate stress levels. The increase in d_{200} as a function of the electric field is predominantly due to the piezoelectric effect, although it also includes a contribution from ferroelectric domain switching, due to the occurrence of residual stress.[9] For $\psi = 90°$, the changes in d_{200} were similar to those described above but opposite in sign. This is expected since the sign of the lateral strains is generally opposite to those of the longitudinal strains.

The results can also be plotted in terms of blocking stress curves. The lattice spacings d_{200} and d_{111} are plotted as a function of the applied, macroscopic stress, as shown in Fig. 10 for $\psi = 0°$. For a given applied electric field, the stress-strain curves are approximately linear. The corresponding fitted lines are shown in the figures. To a first approximation, the slope of the line can be considered independent of the electric field level.

The slope of the blocking stress curves, however, is a function of the azimuthal angle ψ. An illustration is given in Fig. 11(a) for d_{200} and in Fig. 11(b) for d_{111} for an electric field of 2.5 kV/mm. As expected, for orientations approximately aligned with the loading and field axis ($\psi = 0°$), d_{200} decreases with the application of compressive stress, while it increases for orientations close to 90°. As will be explained in Sec. IV, the evolution of this slope can be used to determine the elastic properties and hence anisotropy of the single crystal.

IV. DISCUSSION

As a first assessment of elastic anisotropy, the local strain can be plotted as a function of the applied stress. Fig. 12 shows the local strain obtained from d_{200} measurements for $\psi = 0°$ (black) and the local strain obtained from d_{111} measurements for $\psi = 0°$ (red). The different symbols denote different electric field levels. It can be seen that the strain is essentially linear as a function of the applied stress. The slope of each curve represents an "apparent" Young modulus, often called the diffraction elastic constant.[25] It depends slightly on the electric field level, but the $\langle 111 \rangle$ directions are always stiffer than the $\langle 100 \rangle$ directions. Neglecting this slight variation, the average diffraction elastic constants are 49 and 29 GPa, respectively. It must be noted that this uniform stress assumption (Reuss

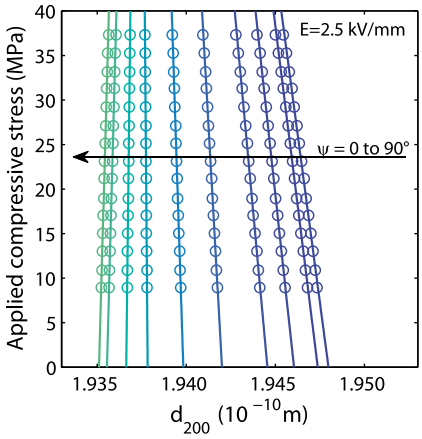

(a) {200} blocking stress curves.

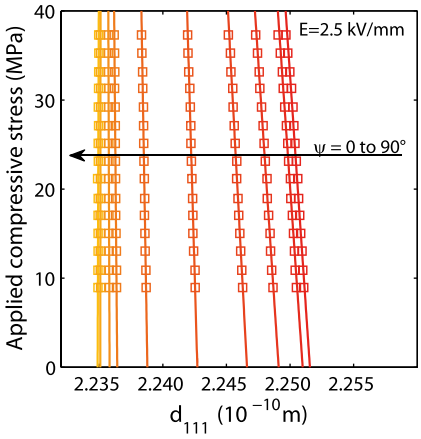

(b) {111} blocking stress curves.

FIG. 11. Analysis of diffraction profiles: blocking stress curves obtained for banks 1 to 10 (corresponding to $\psi = 90°$ to $0°$) for an applied electric field of 2.5 kV/mm. Experimental measurements (markers) and corresponding linear fitting (lines). For the {200} blocking stress curves (a), the sign of the slope changes between $\psi = 60°$ and $\psi = 70°$, while for the {111} blocking stress curves (b), it changes between $\psi = 70°$ and $\psi = 80°$.

approximation) is the simplest approach to the elastic properties of the single crystal, since it neglects stress heterogeneity within the material. It can provide, however, a first estimate of the elastic behaviour. The anisotropy level obtained is very significant. In order to obtain a more accurate estimate of crystalline elastic anisotropy, the Reuss assumption is discarded in the following discussion and an analysis based on more appropriate micro-mechanical tools is proposed.

In order to analyse the data, the sequence of the experiment is described hereafter and illustrated in Fig. 13.

Electric field, total induction, purely dielectric induction, piezoelectric induction, and polarisation are denoted as $\mathbf{E}$, $\mathbf{D}$, $\mathbf{D}^e$, $\mathbf{D}^{pz}$, and $\mathbf{P}$, respectively. They abide by the relation

$$\mathbf{D} = \mathbf{D}^e + \mathbf{D}^{pz} + \mathbf{P}. \tag{1}$$

Stress, total strain, elastic strain, piezoelectric strain, and ferroelectric strain are denoted as $\boldsymbol{\sigma}$, $\boldsymbol{\varepsilon}$, $\boldsymbol{\varepsilon}^e$, $\boldsymbol{\varepsilon}^{pz}$, and $\boldsymbol{\varepsilon}^{fe}$, respectively, and abide by the relation

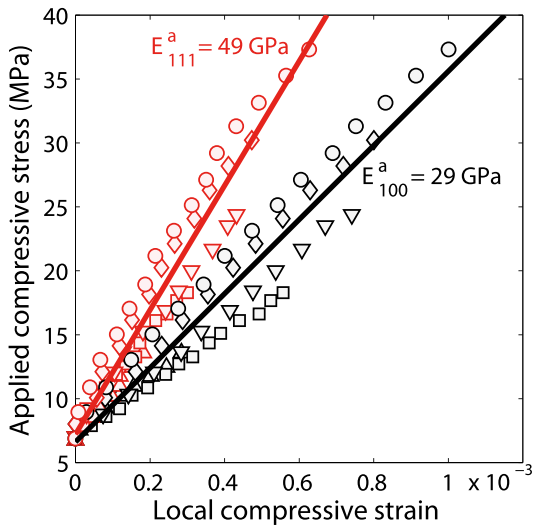

FIG. 12. Local strain (calculated with reference to the lattice spacing after poling) versus applied stress. The results are for $\psi = 0°$. Different markers denote different electric field levels (△, □, ▽, ◇ and ○ denote 0.5, 1, 1.5, 2, and 2.5 kV/mm, respectively). The corresponding apparent Young moduli—or diffraction elastic constants—along ⟨111⟩ and ⟨100⟩ directions underestimate the elastic anisotropy because the applied stress is assumed uniform within the material in this figure (Reuss assumption).

$$\boldsymbol{\varepsilon} = \boldsymbol{\varepsilon}^e + \boldsymbol{\varepsilon}^{pz} + \boldsymbol{\varepsilon}^{fe}. \tag{2}$$

The linear elastic, dielectric, and piezoelectric constitutive laws are written using the compliance tensor $\mathcal{S}$, the permittivity tensor $\boldsymbol{\epsilon}$, and the piezoelectric tensor $\mathbf{d}^{pz}$, where the subscript χ represents the grain scale and the subscript Ω represents the macroscopic scale.

The relationship between the macroscopic stress $\boldsymbol{\sigma}_\Omega$ and the local stress $\boldsymbol{\sigma}_\chi$ is obtained using a micro-mechanical approach.[26] The scale transition rule is given by

$$\boldsymbol{\sigma}_\chi = \mathcal{B}^\sigma_\chi : \boldsymbol{\sigma}_\Omega + \mathcal{L}^\sigma_\chi : \left(\boldsymbol{\varepsilon}^{fe}_\Omega + \boldsymbol{\varepsilon}^{pz}_\Omega - \boldsymbol{\varepsilon}^{fe}_\chi - \boldsymbol{\varepsilon}^{pz}_\chi\right). \tag{3}$$

Similarly, the relationship between the macroscopic electric field $\mathbf{E}_\Omega$ and the local electric field $\mathbf{E}_\chi$ is given by

$$\mathbf{E}_\chi = \mathcal{A}^E_\chi : \mathbf{E}_\Omega + \mathcal{M}^E_\chi : \left(\mathbf{P}_\Omega + \mathbf{D}^{pz}_\Omega - \mathbf{P}_\chi - \mathbf{D}^{pz}_\chi\right). \tag{4}$$

The practical calculation of the localisation operators $\mathcal{B}^\sigma_\chi$, $\mathcal{L}^\sigma_\chi$, $\mathcal{A}^E_\chi$, and $\mathcal{M}^E_\chi$ is summarised in Appendix A.

A. Reference state (state 0)

This state is obtained after poling or repoling of the sample and is the reference state. It was obtained under a fixed compressive preload of approximately 5 MPa, which was

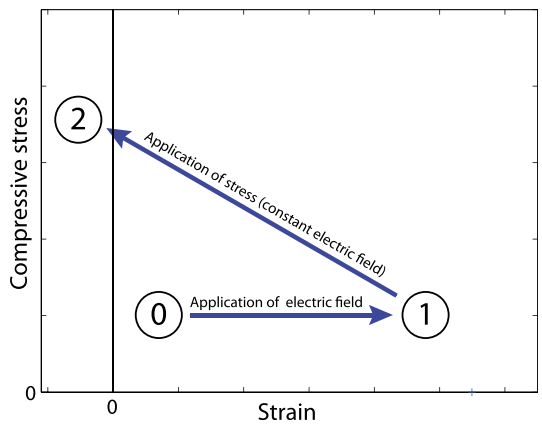

FIG. 13. Schematic view of the experimental procedure.

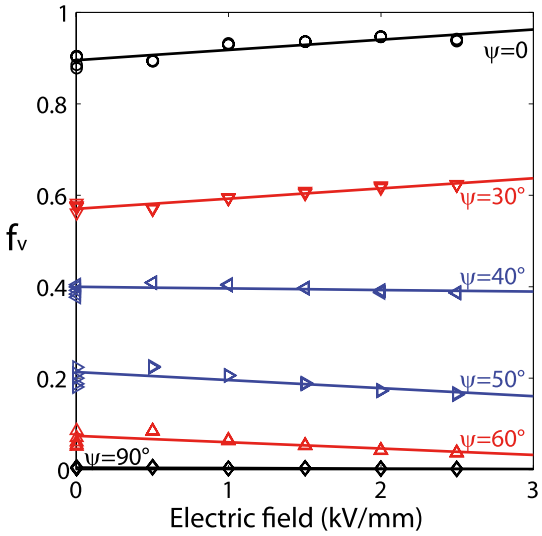

FIG. 14. Volume fraction of domains with polarisation perpendicular to the diffracting plane (111) at stage 1 for several levels of applied electric field and different azimuthal angles ψ. This shows that the volume fractions of ferroelectric domains remain essentially stable when the electric field is applied on the poled sample.

applied in order to ensure contact between the mechanical loading frame and the testing rig.

B. Application of a constant electric field (state 1)

A static electric field $\mathbf{E}_\Omega$ is applied. It is assumed here that the application of this electric field induces little domain switching, which is supported for this experiment by Fig. 14 that shows the evolution of the volume fractions of domains with polarisation perpendicular to the diffracting plane (111). The results are plotted for $\psi = 0°$, 30°, 40°, 50°, 60°, and 90°. This volume fraction, also noted $R_{\{111\}}$,[7,9] is defined by comparison of the (111) and ($\bar{1}11$) peak intensities ($f_v = R_{\{111\}} = I_{(111)}/(I_{(111)} + I_{(\bar{1}11)})$). For $\psi = 0°$, f_v is very high, and on the contrary it is almost zero for $\psi = 90°$ showing that the material was efficiently poled. The volume fraction remains essentially stable irrespective of the electric field subsequently applied, meaning that little further non-180° domain switching occurs when applying the electric field.

C. Application of stress (state 2)

Maintaining the electric field $\mathbf{E}_\Omega$ constant, a uniaxial compressive stress $\boldsymbol{\sigma}_\Omega$ is progressively applied. During this process, it is assumed that, for this material and this range of applied stress, little domain switching is generated by the application of stress. This assumption is supported again by the evolution of the volume fractions of domains with polarisation perpendicular to the diffracting plane (111) as illustrated in Fig. 15. A slight diminution of the volume fraction while the stress increases can be observed for $\psi = 0°$, indicating a stress-induced depoling for this orientation. This domain switching under stress, combined with the residual domain switching observed under electric field for $\psi = 0°$ in Fig. 14, is probably responsible for the variations observed in Fig. 12 between the stress-strain curves at different electric field levels. This amount of domain switching is, however, small and concerns a limited number of orientations close to $\psi = 0°$. It will be neglected as a first approximation.

D. Evolution of lattice spacing d_{hkl} as a function of stress and electric field

Let $\mathbf{z}$ represent the direction of the applied compression, and $\mathbf{u}$ represents the unit vector normal to the considered $\{hkl\}$ planes. The strain ε_{hkl} along direction $\mathbf{u}$ is written as ${}^t\mathbf{u} \,.\, \boldsymbol{\varepsilon}_\chi \,.\, \mathbf{u}$, or

$$\varepsilon_{hkl} = \frac{d_{hkl} - d^0_{hkl}}{d^0_{hkl}}, \tag{5}$$

where d^0_{hkl} is a material constant that refers to the original lattice spacing in the cubic (paraelectric) stress-free reference state.

According to the assumptions made to describe the different stages of the experiment, the local strain $\boldsymbol{\varepsilon}_\chi$ at the grain scale can be calculated (see Appendix B). It is given by

$$\boldsymbol{\varepsilon}_\chi = \mathbf{K}_0 + \mathbf{K}_1(\mathbf{E}_\Omega) + \mathbf{K}_2(\boldsymbol{\sigma}_\Omega), \tag{6}$$

with

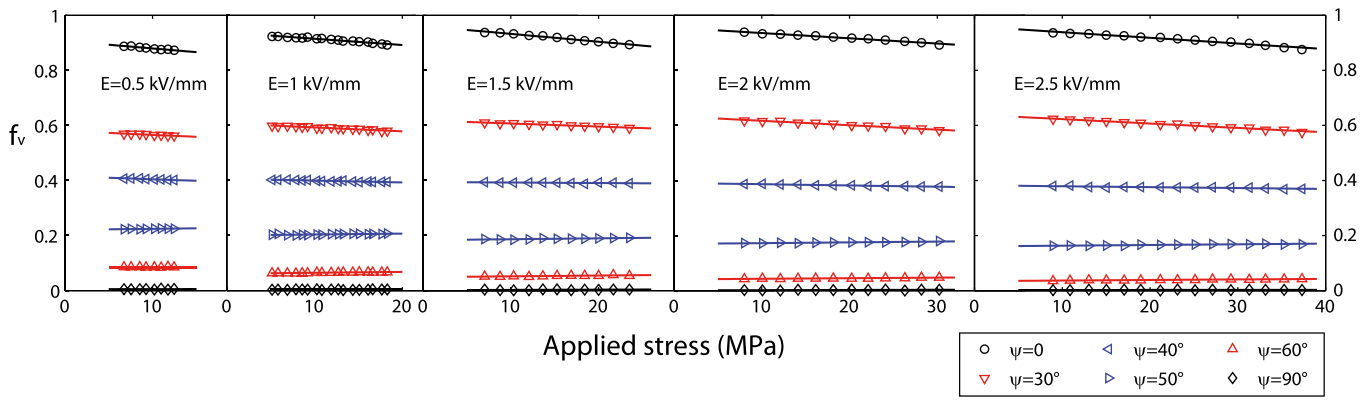

FIG. 15. Volume fraction of domains with polarisation perpendicular to the diffracting plane at stage 2. The results are plotted as a function of the applied stress for several levels of applied electric field and different azimuthal angles ψ. This shows that the volume fractions of ferroelectric domains remain essentially stable when the stress is applied on the poled sample and this is for all the electric field levels.

$$\begin{cases} \mathbf{K}_0 = \boldsymbol{\varepsilon}_\chi^{fe} + \mathcal{S}_\chi : \left(\mathcal{L}_\chi^\sigma : (\boldsymbol{\varepsilon}_\Omega^{fe} - \boldsymbol{\varepsilon}_\chi^{fe})\right) \\ \mathbf{K}_1(\mathbf{E}_\Omega) = {}^t\mathbf{d}_\chi^{pz}.\mathbf{E}_\Omega + \mathcal{S}_\chi : \left(\mathcal{L}_\chi^\sigma : \left(({}^t\mathbf{d}_\Omega^{pz} - {}^t\mathbf{d}_\chi^{pz}).\mathbf{E}_\Omega\right)\right) \cdot \\ \mathbf{K}_2(\boldsymbol{\sigma}_\Omega) = \mathcal{S}_\chi : \left(\mathcal{B}_\chi^\sigma : \boldsymbol{\sigma}_\Omega\right) \end{cases} \tag{7}$$

We then have

$$\frac{d_{hkl}}{d_{hkl}^0} = 1 + {}^t\mathbf{u} \,.\, \mathbf{K}_0 \,.\, \mathbf{u} + {}^t\mathbf{u} \,.\, \mathbf{K}_1(\mathbf{E}_\Omega) \,.\, \mathbf{u} + {}^t\mathbf{u} \,.\, \mathbf{K}_2(\boldsymbol{\sigma}_\Omega) \,.\, \mathbf{u}. \tag{8}$$

At constant stress, the evolution of the lattice parameter with electric field is then a linear function of the piezoelectric and elastic parameters of the single crystal. At constant electric field, the evolution of the lattice parameter with stress is a linear function of the elastic parameters of the single crystal. The latter are the blocking stress curves (Figs. 10 and 11).

E. Blocking stress curves

The blocking stress curve plots the variation of lattice spacing d_{hkl} from state 1 to state 2 as a function of the amplitude of the applied uniaxial compressive stress $\boldsymbol{\sigma}_\Omega$. It is thus a plot of ${}^t\mathbf{z} \,.\, \boldsymbol{\sigma}_\Omega \,.\, \mathbf{z}$ as a function of $d_{hkl}^0(1 + {}^t\mathbf{u} \,.\, \boldsymbol{\varepsilon}_\chi \,.\, \mathbf{u})$ and can be used to determine the single crystal stiffness tensor. The slope $1/p$ of the blocking stress curves is given by

$$p = \frac{\partial d_{hkl}}{\partial \sigma} = d_{hkl}^0 \, {}^t\mathbf{u} \,.\, \left(\mathcal{S}_\chi : (\mathcal{B}_\chi^\sigma : \boldsymbol{\sigma}_\Omega)\right) . \mathbf{u}. \tag{9}$$

The applied stress being a uniaxial compression of amplitude σ along $\mathbf{z}$, it can be expressed as

$$\boldsymbol{\sigma}_\Omega = \sigma \; \mathbf{z} \otimes \mathbf{z}. \tag{10}$$

We then have

$$p = d_{hkl}^0 \, {}^t\mathbf{u} \,.\, \left(\mathcal{S}_\chi : (\mathcal{B}_\chi^\sigma : \mathbf{z} \otimes \mathbf{z})\right) . \mathbf{u}. \tag{11}$$

For a given crystallographic orientation and for a given projection direction $\mathbf{u}$ (corresponding to a given plane $\{hkl\}$), this slope is a constant. This corresponds well with experimental results showing that blocking stress curves for a given orientation are parallel lines (Fig. 10), but that the slope depends on the orientation (Fig. 11). If we assume that the elastic coefficients show a cubic symmetry and are uniform within a grain, and that the polycrystal is macroscopically isotropic, analytical solutions can be found for this expression of the slope. The details of calculation are given in Appendix C.

Two important results are obtained when considering the diffracting planes {200} and {111}. In this case, p is a linear function of the square cosine of the azimuthal angle ψ. The expression of these slopes are given by

$$p_{200} = \alpha_{200} + \beta_{200} \cos^2\psi, \tag{12}$$

$$p_{111} = \alpha_{111} + \beta_{111} \cos^2\psi, \tag{13}$$

with

$$\begin{cases} \alpha_{200} = d_{200}^0 \left(\dfrac{1}{9k} - \dfrac{\mu_\Omega + \mu^*}{6\mu_\Omega(\mu_a + \mu^*)}\right) \\ \beta_{200} = d_{200}^0 \dfrac{\mu_\Omega + \mu^*}{2\mu_\Omega(\mu_a + \mu^*)} \\ \alpha_{111} = d_{111}^0 \left(\dfrac{1}{9k} - \dfrac{\mu_\Omega + \mu^*}{6\mu_\Omega(\mu_b + \mu^*)}\right) \\ \beta_{111} = d_{111}^0 \dfrac{\mu_\Omega + \mu^*}{2\mu_\Omega(\mu_b + \mu^*)} \end{cases}, \tag{14}$$

where μ_a, μ_b, and k are the two shear moduli and the bulk modulus of the single crystal (assuming a cubic symmetry), μ_Ω is the shear modulus of the polycrystal that can be obtained from the resolution of a homogenisation problem (assuming a macroscopic isotropic elastic behaviour), and μ^* is the shear modulus of the Hill constraint tensor in this homogenisation problem (see Appendix C). The azimuthal angles ψ_{200}^v and ψ_{111}^v for which {200} and {111} blocking stress curves are vertical lines can be easily determined from (12) and (13)

$$\psi_{200}^v = \cos^{-1}\sqrt{-\frac{\alpha_{200}}{\beta_{200}}}, \tag{15}$$

$$\psi_{111}^v = \cos^{-1}\sqrt{-\frac{\alpha_{111}}{\beta_{111}}}. \tag{16}$$

The experimental curves of p_{200} and p_{111} as a function of $\cos^2\psi$ are given in Fig. 16. For a given electric field level, it is verified with very good accuracy that p_{200} and p_{111} are linear functions of $\cos^2\psi$, but a slight dependence on the electric field is obtained as illustrated in Fig. 17. The horizontal line represents the average values for α_{200}, β_{200}, α_{111}, and β_{111}. This dependence on electric field can probably be attributed to the residual domain switching neglected in the modelling process.

The identified values for α_{200}, β_{200}, α_{111}, and β_{111} are given in Table I. The corresponding values for ψ_{200}^v and ψ_{111}^v are also reported. They are consistent with the results of Fig. 11.

F. Practical identification of single crystal elastic coefficients

Once the parameters α_{200}, β_{200}, α_{111}, and β_{111} have been identified (Table I), a procedure to identify the single crystal elastic coefficients can be defined from the set of equations (14). In the reference cubic state, d_{hkl}^0 is defined by

$$d_{hkl}^0 = \frac{a^0}{\sqrt{h^2 + k^2 + l^2}}, \tag{17}$$

where a^0 is the lattice parameter of this reference cubic state. It is then easily shown that

$$\frac{d_{200}^0}{d_{111}^0} = \frac{\sqrt{3}}{2}, \tag{18}$$

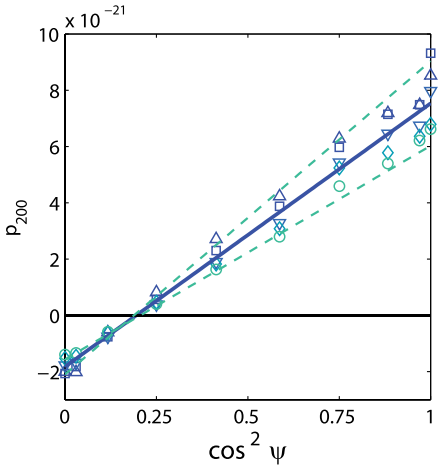

(a) Slope p_{200} of the {200} blocking stress curves (unit : $m^2.s^2.kg^{-1}$).

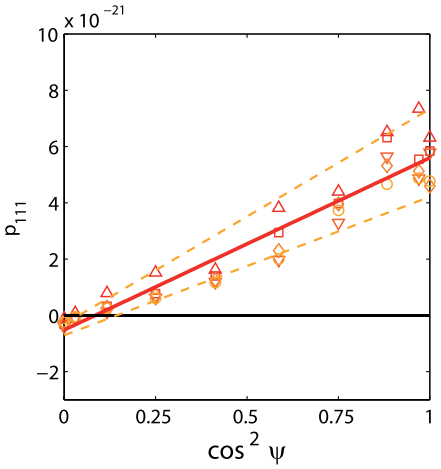

(b) Slope p_{111} of the {111} blocking stress curves (unit : $m^2.s^2.kg^{-1}$).

FIG. 16. Slope of the blocking stress curves as a function of $\cos^2\psi$ and corresponding linear fitting. Markers △, □, ▽, ◇, and ○ denote results at 0.5, 1, 1.5, 2, and 2.5 kV/mm, respectively.

so that the following relation must be verified by the identified parameters of Table I:

$$\frac{\alpha_{200}+\beta_{200}/3}{\alpha_{111}+\beta_{111}/3}=\frac{\sqrt{3}}{2}. \tag{19}$$

In the case studied here, the ratio is found to be equal to 0.87, corresponding to an error less than 0.5%.

Moreover, assuming that the transformation from the initial cubic state to the ferroelectric state is isochoric, the lattice parameter a^0 can be defined as

$$a^0=a\sqrt[3]{\cos^2\delta} \tag{20}$$

for rhombohedral materials (where a is the lattice parameter and δ is the standard distorsion angle of the rhombohedral phase) or as

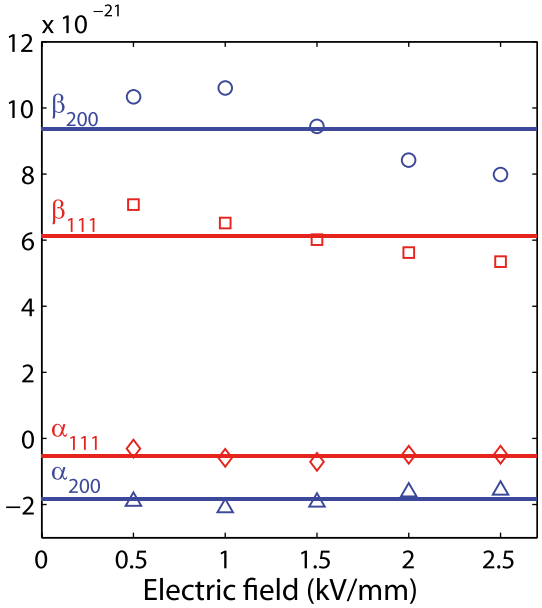

FIG. 17. Values identified for α_{200}, β_{200}, α_{111}, and β_{111} as a function of the applied electric field (unit : $m^2\cdot s^2\cdot kg^{-1}$). The values were obtained from the linear fitting of p_{200} and p_{111} as a function of $\cos^2\psi$.

$$a^0=\sqrt[3]{ac^2} \tag{21}$$

for tetragonal materials (where a and c are the standard lattice parameters of the tetragonal phase). Note that the constant volume assumption is only used as an approximation for the paraelectric to ferroelectric transformation in order to define the lattice parameter a^0. In the remainder of the paper, the sample volume is not constant, notably due to the significant elastic contribution.

The ratio β_{111}/β_{200} provides an estimate of the single crystal anisotropy. In actual fact, it will systematically underestimate the single crystal anisotropy since μ^* is always positive. It is recalled that single crystal isotropy is found for $\mu_a=\mu_b$

$$\begin{aligned}&\frac{\sqrt{3}}{2}\frac{\beta_{111}}{\beta_{200}}=\frac{\mu_a+\mu^*}{\mu_b+\mu^*}<\frac{\mu_a}{\mu_b} \quad \text{if} \quad \mu_a>\mu_b,\\ &\text{or}\\ &\frac{\sqrt{3}}{2}\frac{\beta_{111}}{\beta_{200}}=\frac{\mu_a+\mu^*}{\mu_b+\mu^*}>\frac{\mu_a}{\mu_b} \quad \text{if} \quad \mu_a<\mu_b.\end{aligned} \tag{22}$$

For the material studied here, it is found that the anisotropy ratio is lower than 0.566, indicative of very significant anisotropy (see Ref. 26).

Given the lattice parameter a^0 for the reference state, the elastic coefficients of the single crystal can be identified. Since the expressions of μ_Ω and μ^* depend on μ_a, μ_b, and k, a simple fixed point algorithm can be developed, provided in Appendix D. The solution obtained for the material studied in this paper is given in Table II. The calculation has been made for $a^0=3.9$ Å. According to Fig. 8, a^0 could lie between 3.87 and 3.90 Å, but the results show very little sensitivity to a^0 in this range. The error bars given in Table II

TABLE I. Values of α_{200}, β_{200}, α_{111}, and β_{111} identified from the slopes of the blocking stress curves obtained from the high energy x-ray diffraction experiments. Unit: $m^2\cdot s^2\cdot kg^{-1}$. The calculated azimuthal angles ψ^v_{200} and ψ^v_{111} for which {200} and {111} blocking stress curves are vertical lines are also reported.

Parameter	α_{200} (10^{-21})	β_{200} (10^{-21})	α_{111} (10^{-21})	β_{111} (10^{-21})	ψ^v_{200}	ψ^v_{111}
Value	−1.8±0.3	9.4±1.4	−0.5±0.2	6.1±1.0	63°	72°

TABLE II. Elastic coefficients of PZT 55-45 single crystal.

Parameter	a^0	k	μ_a	μ_b	μ_a/μ_b	E_{200}/E_{111}
Value	3.9	16.3±3.2	6.8±1.4	22.7±3.5	0.30±0.04	0.25±0.04
Unit	Å	GPa	GPa	GPa	…	…

have been obtained by considering independently the results from each value of the electric field. It is recalled that the results were obtained assuming negligible domain switching during the blocking stress experiment. It is worth noting that if such domain switching under stress was significant, it would affect mostly the {111} strain curves for a rhombohedral perovskite ferroelectric and would tend to make them appear more compliant than they are. Consequently, neglecting the domain switching contribution tends to underestimate the crystalline elastic anisotropy in the present case.

The model, in a simplified version, could also be used to identify the material properties directly from measurements on single crystals. Single crystals, however, can be difficult to obtain. The idea here is to show that the synthesis of single crystals can be avoided by combining *in-situ* measurements on polycrystals and appropriate micro-mechanical modelling.

The anisotropy ratio of 0.30 ± 0.04 found for PZT 55-45 is very significant and deviates further from the isotropic value of 1 than that of pure iron (0.41) or nickel (0.40), for example. This questions most of the modelling approaches for ferroelectric behaviour that neglect this local elastic anisotropy.[27,28] Indeed, as shown in the previous studies,[26,29] a strong local anisotropy has a significant impact both on the macroscopic response and on the development of internal stresses in ferroelectric materials under electromechanical loading.

V. CONCLUSION

High energy x-ray diffraction experiments have been carried out on a rhombohedral PZT piezoelectric ceramic. *In-situ* blocking stress curves have been obtained from these measurements for the lattice spacings d_{200} and d_{111}. These blocking stress curves were found to be approximately linear. Using a micromechanical analysis and experimental data in which little non-180° domain switching occurred, the single crystal elastic coefficients have been determined. The crystal elastic behaviour appears to be highly anisotropic. This local anisotropy plays a significant role in the development of internal stresses in ferroelectric ceramics and should, therefore, be introduced when modelling ferroelectric behaviour. The local elastic coefficients derived from this approach can be used to evaluate other practical cases where non-180° domain switching is more significant. In such a case, a more complicated modelling approach based on a micromechanical analysis of domain switching processes[26] would be necessary. In a similar manner, the anisotropic piezoelectric coefficients could be obtained by studying "blocking field" experiments under static stress.

ACKNOWLEDGMENTS

The authors are grateful for support provided by the ESRF under Grant No. MA-1727, "Ferroelectric-ferroelastic domain switching and the blocking stress in piezoelectric ceramics." This work was supported at the University of Manchester by the Engineering and Physical Sciences Research Council (EPSRC) under the Grant No. EP/J010685/1. L.D. gratefully acknowledges sabbatical leave support granted by Univ Paris-Sud. The authors also gratefully acknowledge Andreja Benčan and Barbara Malič for processing the PZT ceramics. K.G.W. would also like to acknowledge the Deutsche Forschungsgemeinschaft (DFG) under SFB 595/D6.

APPENDIX A: CALCULATION OF THE LOCALISATION OPERATORS

1. Mechanical localisation operators

The calculation of the localisation tensor $\mathcal{B}_\chi^\sigma$ requires several intermediate steps. The calculation is based on the resolution of an Eshelby's inclusion problem. The Eshelby tensor $\mathcal{N}_\chi$ corresponding to the inclusion problem is calculated first.[33] It depends on the shape of the inclusion and on the elastic properties of the infinite medium surrounding the inclusion. The shape of the inclusion is representative of the phase distribution.[30] For polycrystals, a phase can be defined as the set of grains having a specific crystallographic orientation. If the spatial distribution of a phase is isotropic, a spherical inclusion is chosen. In the case of a self-consistent calculation, the elastic stiffness tensor of the infinite medium is the self-consistent estimate $\tilde{\mathcal{C}}_\Omega$. The monograph by Mura[34] provides the guidelines for the practical calculation of the Eshelby tensor $\mathcal{N}_\chi$. The Hill constraint tensor $\mathcal{C}_\chi^*$ is then defined (A1), from which the strain localisation tensor $\mathcal{A}_\chi^\sigma$ (A2) and the stress concentration tensor $\mathcal{B}_\chi^\sigma$ are deduced (A3). $\mathcal{I}$ is the fourth order identity tensor. The incompatibility tensor $\mathcal{L}_\chi^\sigma$ is finally calculated (A4)

$$\mathcal{C}_\chi^* = \tilde{\mathcal{C}}_\Omega : \left(\mathcal{N}_\chi{}^{-1} - \mathcal{I}\right), \tag{A1}$$

$$\mathcal{A}_\chi^\sigma = \left(\mathcal{C}_\chi + \mathcal{C}_\chi^*\right)^{-1} : \left(\tilde{\mathcal{C}}_\Omega + \mathcal{C}_\chi^*\right), \tag{A2}$$

$$\mathcal{B}_\chi^\sigma = \mathcal{C}_\chi : \mathcal{A}_\chi^\sigma : \tilde{\mathcal{C}}_\Omega{}^{-1}, \tag{A3}$$

$$\mathcal{L}_\chi^\sigma = \left(\mathcal{C}_\chi^{-1} + \mathcal{C}_\chi^{*-1}\right)^{-1}. \tag{A4}$$

2. Electric localisation operators

The same approach applies for the electric field localisation. The depolarising tensor $\mathbf{N}_\chi$ is calculated first (see, for instance, the monographs by Sihvola[35] or Milton[36]). The self-consistent estimate $\tilde{\boldsymbol{\epsilon}}_\Omega$ for the dielectric permittivity is also used. The intermediate tensor $\boldsymbol{\epsilon}_\chi^*$ and localisation operators $\mathcal{A}_\chi^E$ and $\mathcal{B}_\chi^E$ are then calculated. $\mathbf{I}$ is the second order identity tensor. The incompatibility tensor $\mathcal{M}_\chi^E$ is finally calculated (A8)

$$\boldsymbol{\epsilon}_\chi^* = \tilde{\boldsymbol{\epsilon}}_\Omega : \left(\mathbf{N}_\chi{}^{-1} - \mathbf{I}\right), \tag{A5}$$

$$\mathcal{A}_\chi^E = \left(\boldsymbol{\epsilon}_\chi + \boldsymbol{\epsilon}_\chi^*\right)^{-1} : \left(\tilde{\boldsymbol{\epsilon}}_\Omega + \boldsymbol{\epsilon}_\chi^*\right), \tag{A6}$$

$$\mathcal{B}_\chi^E = \boldsymbol{\epsilon}_\chi : \mathcal{A}_\chi^E : \tilde{\boldsymbol{\epsilon}}_\Omega{}^{-1}, \tag{A7}$$

$$\mathcal{M}_\chi^E = \left(\boldsymbol{\epsilon}_\chi + \boldsymbol{\epsilon}_\chi^*\right)^{-1}. \tag{A8}$$

A detailed explanation for the definition of scale transition rules in the case of coupled behaviour can be found in Ref. 32.

APPENDIX B: CALCULATION OF THE LOCAL STRAIN AT THE GRAIN SCALE AS A FUNCTION OF STRESS AND ELECTRIC FIELD

In this appendix, we derive the expression of the local strain tensor $\boldsymbol{\varepsilon}_\chi$ at the grain scale as a function of the macroscopic applied stress $\boldsymbol{\sigma}_\Omega$ and electric field $\mathbf{E}_\Omega$. We refer to the loading sequence defined in Sec. IV (Fig. 13) and make use of the decomposition (2), of the single crystal constitutive law and of the scale transition rule (3)

$$\begin{aligned}\boldsymbol{\varepsilon}_\chi &= \boldsymbol{\varepsilon}_\chi^{fe} + \boldsymbol{\varepsilon}_\chi^{pz} + \boldsymbol{\varepsilon}_\chi^{e} \\ &= \boldsymbol{\varepsilon}_\chi^{fe} + {}^t\mathbf{d}_\chi^{pz}.\mathbf{E}_\chi + \mathcal{S}_\chi : \boldsymbol{\sigma}_\chi \\ &= \boldsymbol{\varepsilon}_\chi^{fe} + {}^t\mathbf{d}_\chi^{pz}.\mathbf{E}_\chi \\ &\quad + \mathcal{S}_\chi : \left(\mathcal{B}_\chi^\sigma : \boldsymbol{\sigma}_\Omega + \mathcal{L}_\chi^\sigma : (\boldsymbol{\varepsilon}_\Omega^{fe} + \boldsymbol{\varepsilon}_\Omega^{pz} - \boldsymbol{\varepsilon}_\chi^{fe} - \boldsymbol{\varepsilon}_\chi^{pz})\right),\end{aligned} \tag{B1}$$

which can be written in the following form:

$$\begin{aligned}\boldsymbol{\varepsilon}_\chi &= \boldsymbol{\varepsilon}_\chi^{fe} + \mathcal{S}_\chi : \left(\mathcal{L}_\chi^\sigma : (\boldsymbol{\varepsilon}_\Omega^{fe} - \boldsymbol{\varepsilon}_\chi^{fe})\right) \\ &\quad + {}^t\mathbf{d}_\chi^{pz}.\mathbf{E}_\chi + \mathcal{S}_\chi : \left(\mathcal{L}_\chi^\sigma : ({}^t\mathbf{d}_\Omega^{pz}.\mathbf{E}_\Omega - {}^t\mathbf{d}_\chi^{pz}.\mathbf{E}_\chi)\right) \\ &\quad + \mathcal{S}_\chi : \left(\mathcal{B}_\chi^\sigma : \boldsymbol{\sigma}_\Omega\right).\end{aligned} \tag{B2}$$

If we assume that no domain switching has occurred during the process, the first line of (B2) is a constant from stage 0, noted as $\mathbf{K}_0$ and assumed independent of both stress and electric field. It is assumed that the electric field is uniform within the material ($\mathbf{E}_\chi = \mathbf{E}_\Omega$), which means that the second line of (B2) is a linear function of the applied electric field $\mathbf{E}_\Omega$, noted as $\mathbf{K}_1(\mathbf{E}_\Omega)$. The third line of (B2) is a linear function of $\boldsymbol{\sigma}_\Omega$, noted as $\mathbf{K}_2(\boldsymbol{\sigma}_\Omega)$. The expression of $\boldsymbol{\varepsilon}_\chi$ is then given by

$$\boldsymbol{\varepsilon}_\chi = \mathbf{K}_0 + \mathbf{K}_1(\mathbf{E}_\Omega) + \mathbf{K}_2(\boldsymbol{\sigma}_\Omega), \tag{B3}$$

with

$$\begin{cases}\mathbf{K}_0 = \boldsymbol{\varepsilon}_\chi^{fe} + \mathcal{S}_\chi : \left(\mathcal{L}_\chi^\sigma : (\boldsymbol{\varepsilon}_\Omega^{fe} - \boldsymbol{\varepsilon}_\chi^{fe})\right) \\ \mathbf{K}_1(\mathbf{E}_\Omega) = {}^t\mathbf{d}_\chi^{pz}.\mathbf{E}_\Omega + \mathcal{S}_\chi : \left(\mathcal{L}_\chi^\sigma : \left(({}^t\mathbf{d}_\Omega^{pz} - {}^t\mathbf{d}_\chi^{pz}).\mathbf{E}_\Omega\right)\right) \\ \mathbf{K}_2(\boldsymbol{\sigma}_\Omega) = \mathcal{S}_\chi : \left(\mathcal{B}_\chi^\sigma : \boldsymbol{\sigma}_\Omega\right)\end{cases}. \tag{B4}$$

APPENDIX C: CALCULATION OF THE SLOPE OF THE BLOCKING STRESS CURVES

The slope $1/p$ of a blocking stress curves is given by (11) recalled hereafter

$$p = d_{hkl}^0 {}^t\mathbf{u}.\left(\mathcal{S}_\chi : (\mathcal{B}_\chi^\sigma : \mathbf{z}\otimes\mathbf{z})\right).\mathbf{u}. \tag{C1}$$

The objective of this appendix is to express p as a function of the elastic parameters of the single crystal thanks to an explicit calculation of $\mathcal{B}_\chi^\sigma$. For the following, it is convenient to introduce the base tensors $(\mathcal{J},\mathcal{K})$ for isotropic fourth rank tensors and the base tensors $(\mathcal{J},\mathcal{K}_a,\mathcal{K}_b)$ for cubic fourth rank tensors[31] (δ is the Kronecker symbol)

$$\begin{cases}\mathcal{J}_{ijkl} = \dfrac{1}{3}\delta_{ij}\delta_{kl} \\ \mathcal{I}_{ijkl} = \dfrac{1}{2}(\delta_{ik}\delta_{jl} + \delta_{il}\delta_{jk}) \\ \mathcal{P}_{ijkl} = \delta_{ij}\delta_{kl}\delta_{ik} \\ \mathcal{K}_a = \mathcal{P} - \mathcal{J} \\ \mathcal{K}_b = \mathcal{I} - \mathcal{P} \\ \mathcal{K} = \mathcal{K}_a + \mathcal{K}_b.\end{cases} \tag{C2}$$

We assume that the elastic symmetry is cubic at the single crystal scale. The elastic stiffness tensor $\mathcal{S}_\chi$ can then be written

$$\mathcal{S}_\chi = \frac{1}{3k}\mathcal{J} + \frac{1}{2\mu_a}\mathcal{K}_a + \frac{1}{2\mu_b}\mathcal{K}_b, \tag{C3}$$

where k is the bulk modulus, μ_a and μ_b are the two shear moduli that describes the crystal anisotropy (the anisotropy ratio can be defined as μ_a/μ_b). These coefficients can also be defined from the stiffness tensor $\mathcal{C}_\chi$ of the single crystal

$$\begin{cases}\mu_a = \dfrac{1}{2}(\mathcal{C}_{\chi_{1111}} - \mathcal{C}_{\chi_{1122}}) \\ \mu_b = \mathcal{C}_{\chi_{2323}} \\ k = \dfrac{1}{3}(\mathcal{C}_{\chi_{1111}} + 2\mathcal{C}_{\chi_{1122}}).\end{cases} \tag{C4}$$

The macroscopic elastic compliance tensor $\mathcal{S}_\Omega$ is taken to be isotropic. It is written

$$\mathcal{S}_\Omega = \frac{1}{3k_\Omega}\mathcal{J} + \frac{1}{2\mu_\Omega}\mathcal{K}, \tag{C5}$$

where k_Ω and μ_Ω are, respectively, the bulk and shear modulus of the isotropic polycrystal. They can be obtained from a macroscopic measurement. They relate to Young's modulus E_Ω and Poisson's ratio ν_Ω by

$$\mu_\Omega = \frac{E_\Omega}{2(1+\nu_\Omega)} \quad \text{and} \quad k_\Omega = \frac{E_\Omega}{3(1-2\nu_\Omega)}. \tag{C6}$$

The macroscopic elastic parameters can also be obtained from an homogenisation approach.[30] k_Ω and μ_Ω are then given by

$$\mu_\Omega = \frac{5(\mu_a+\mu^*)(\mu_b+\mu^*)}{3\mu_a + 2\mu_b + 5\mu^*} - \mu^* \quad \text{and} \quad k_\Omega = k. \tag{C7}$$

This expression introduces the—isotropic—Hill tensor $\mathcal{C}^*$ (Ref. 30)

$$\mathcal{C}^* = 3k^*\mathcal{J} + 2\mu^*\mathcal{K}, \tag{C8}$$

with

$$2\mu^* = \frac{\mu^\infty(9k^\infty + 8\mu^\infty)}{3(k^\infty + 2\mu^\infty)} \quad \text{and} \quad 3k^* = 4\mu^\infty, \tag{C9}$$

where μ^∞ and k^∞ are the properties used for the infinite medium for the Eshelby's inclusion problem in the Hill approach. The self-consistent method being chosen in the following, we will use $\mu^\infty = \mu_\Omega$ and $k^\infty = k_\Omega$.

The localisation operator $\mathcal{B}^\sigma_\chi$ is then defined by

$$\mathcal{B}^\sigma_\chi = \mathcal{C}_\chi : \mathcal{A}^\sigma_\chi : \mathcal{C}^{-1}_\Omega, \tag{C10}$$

with

$$\mathcal{A}^\sigma_\chi = \left(\mathcal{C}_\chi + \mathcal{C}^*\right)^{-1} : \left(\mathcal{C}_\Omega + \mathcal{C}^*\right). \tag{C11}$$

All calculations done, we obtain

$$\mathcal{B}^\sigma_\chi = \mathcal{J} + \frac{\mu_a(\mu_\Omega + \mu^*)}{\mu_\Omega(\mu_a + \mu^*)}\mathcal{K}_a + \frac{\mu_b(\mu_\Omega + \mu^*)}{\mu_\Omega(\mu_b + \mu^*)}\mathcal{K}_b. \tag{C12}$$

The expression of the slope p can then be developed, and leads to (C13)

$$p = d^0_{hkl}\left(\frac{1}{9k} + \frac{\mu_\Omega + \mu^*}{2\mu_\Omega(\mu_a + \mu^*)}(u_i^2 z_i^2 - 1/3) + \frac{\mu_\Omega + \mu^*}{2\mu_\Omega(\mu_b + \mu^*)}(1 - \delta_{ij})u_i u_j z_i z_j\right). \tag{C13}$$

In this expression, **u** is the unit vector normal to the diffracting plane $\{hkl\}$, and **z** is the direction of the applied stress. In a coordinate system (**u**,**v**,**w**) attached to the diffracting plane (Fig. 18), **z** can be expressed

$$\mathbf{z} = \cos\psi\,\mathbf{u} + \sin\psi\cos\theta\,\mathbf{v} + \sin\psi\sin\theta\,\mathbf{w}. \tag{C14}$$

In the general case, the expression for p will depend not only on the azimuthal angle ψ but also on the rotation angle θ (several crystallographic orientations correspond to a given diffracting plane, and the stress is not uniform within all these orientations). However, for two particular diffracting planes, $\{200\}$ and $\{111\}$, this angle θ is eliminated in the equations.

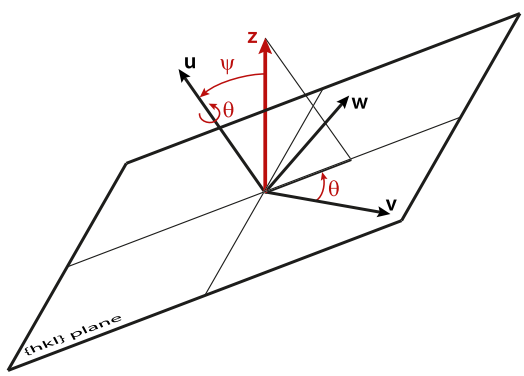

FIG. 18. Schematic view of the angles and coordinate systems used in the calculation.

1. {200} diffraction

If $\{200\}$ is the diffracting plane, a possible choice for (**u**,**v**,**w**) is

$$\mathbf{u} = \begin{vmatrix}1\\0\\0\end{vmatrix}, \quad \mathbf{v} = \begin{vmatrix}0\\1\\0\end{vmatrix}, \quad \mathbf{w} = \begin{vmatrix}0\\0\\1\end{vmatrix}, \tag{C15}$$

leading to

$$p_{200} = d^0_{200}\left(\frac{1}{9k} + \frac{\mu_\Omega + \mu^*}{2\mu_\Omega(\mu_a + \mu^*)}(\cos^2\psi - 1/3)\right). \tag{C16}$$

It is worth noting that if a uniform stress assumption is used (Reuss assumption), $\mu^* = 0$ and the expression reduces to

$$p^R_{200} = d^0_{200}\left(\frac{1}{9k} + \frac{1}{2\mu_a}(\cos^2\psi - 1/3)\right). \tag{C17}$$

2. {111} diffraction

If $\{111\}$ is the diffracting plane, a possible choice for (**u**,**v**,**w**) is

$$\mathbf{u} = \frac{1}{\sqrt{3}}\begin{vmatrix}1\\1\\1\end{vmatrix}, \quad \mathbf{v} = \frac{1}{\sqrt{2}}\begin{vmatrix}1\\-1\\0\end{vmatrix}, \quad \mathbf{w} = \frac{1}{\sqrt{6}}\begin{vmatrix}1\\1\\-2\end{vmatrix}, \tag{C18}$$

leading to

$$p_{111} = d^0_{111}\left(\frac{1}{9k} + \frac{\mu_\Omega + \mu^*}{2\mu_\Omega(\mu_b + \mu^*)}(\cos^2\psi - 1/3)\right). \tag{C19}$$

Again it is noteworthy that if a uniform stress assumption is used (Reuss assumption), $\mu^* = 0$ and the expression reduces to

$$p^R_{111} = d^0_{111}\left(\frac{1}{9k} + \frac{1}{2\mu_b}(\cos^2\psi - 1/3)\right). \tag{C20}$$

Expressions (C16) and (C19) can be used to identify the elastic parameters k, μ_a, and μ_b of the single crystal.

APPENDIX D: FIXED POINT ALGORITHM FOR THE DETERMINATION OF THE SINGLE CRYSTAL ELASTIC COEFFICIENTS

The algorithm for the determination of μ_a, μ_b, and k from (14) and the knowledge of the parameter a^0 can be defined as follows.

- Identification of α_{200}, β_{200}, α_{111}, and β_{111} from the Blocking stress curves.
- Determination of d^0_{200} and d^0_{111} from a^0 (17).
- Initial guess for μ_Ω and μ^* (from the approximate knowledge of the macroscopic coefficients, and using (C9)).
- Determination of k:

$$k = \frac{2}{9\left(\frac{\alpha_{200} + \beta_{200}/3}{d^0_{200}} + \frac{\alpha_{111} + \beta_{111}/3}{d^0_{111}}\right)}. \tag{D1}$$

- Initialisation: $\zeta^0 = 10^{-3}$, $\zeta = 1$, $\mu_a^r = 1$, $\mu_b^r = 1$.
- While $\zeta > \zeta^0$
  (i) Calculation of μ_a:

$$\mu_a = \frac{d_{200}^0}{2\beta_{200}}\left(1 + \frac{\mu^*}{\mu_\Omega}\right) - \mu^*. \tag{D2}$$

  (ii) Calculation of μ_b:

$$\mu_b = \frac{d_{111}^0}{2\beta_{111}}\left(1 + \frac{\mu^*}{\mu_\Omega}\right) - \mu^*. \tag{D3}$$

  (iii) Calculation of the convergence indicator:

$$\zeta = 100 \times \frac{|\mu_a - \mu_a^r|}{\mu_a^r} + 100 \times \frac{|\mu_b - \mu_b^r|}{\mu_b^r}. \tag{D4}$$

  (iv) $\mu_a^r = \mu_a$, $\mu_b^r = \mu_b$.
  (v) Updating of μ_Ω (C7) and μ^* (C9).
- Solution (μ_a, μ_b, k).

[1]D. Damjanovic, Rep. Prog. Phys. **61**, 1267–1324 (1998).
[2]D. Damjanovic, J. Appl. Phys. **82**, 1788–1797 (1997).
[3]D. A. Hall, J. Mater. Sci. **36**, 4575–4601 (2001).
[4]R. E. Eitel, T. R. Shrout, and C. A. Randall, J. Appl. Phys. **99**, 124110 (2006).
[5]P. Yang and D. A. Payne, J. Appl. Phys. **71**, 1361–1367 (1992).
[6]X. Tan, C. Ma, J. Frederick, S. Beckman, and K. G. Webber, J. Am. Ceram. Soc. **94**, 4091–4107 (2011).
[7]D. A. Hall, A. Steuwer, B. Cherdhirunkorn, T. Mori, and P. J. Withers, J. Appl. Phys. **96**, 4245–4252 (2004).
[8]D. A. Hall, A. Steuwer, B. Cherdhirunkorn, P. J. Withers, and T. Mori, J. Mech. Phys. Solids **53**, 249–260 (2005).
[9]D. A. Hall, A. Steuwer, B. Cherdhirunkorn, T. Mori, and P. J. Withers, Acta Mater. **54**, 3075–3083 (2006).
[10]J. L. Jones, B. J. Iverson, and K. J. Bowman, J. Am. Ceram. Soc. **90**, 2297–2314 (2007).
[11]K. A. Schönau, M. Knapp, H. Kungl, M. J. Hoffmann, and H. Fuess, Phys. Rev. B **76**, 144112 (2007).
[12]A. K. Singh, S. K. Mishra, Ragini, D. Pandey, S. Yoon, S. Baik, and N. Shin, Appl. Phys. Lett. **92**, 022910 (2008).
[13]A. Pramanick, J. E. Daniels, and J. L. Jones, J. Am. Ceram. Soc. **92**, 2300–2310 (2009).
[14]A. Pramanick, D. Damjanovic, J. E. Daniels, J. C. Nino, and J. L. Jones, J. Am. Ceram. Soc. **94**, 293–309 (2011).
[15]J. E. Daniels, W. Jo, J. Rödel, V. Honkimäki, and J. L. Jones, Acta Mater. **58**, 2103–2111 (2010).
[16]W. Jo, R. Dittmer, M. Acosta, J. Zang, C. Groh, E. Sapper, K. Wang, and J. Rödel, J. Electroceram. **29**, 71–93 (2012).
[17]K. G. Webber, E. Aulbach, and J. Rödel, J. Phys. D: Appl. Phys. **43**, 365401 (2010).
[18]R. Dittmer, K. G. Webber, E. Aulbach, W. Jo, X. Tan, and J. Rödel, Sens. Actuators, A **189**, 187–194 (2013).
[19]Y. H. Seo, A. Benčan, J. Koruza, B. Malič, M. Kosec, and K. G. Webber, J. Am. Ceram. Soc. **94**(12), 4419–4425 (2011).
[20]Y. H. Seo, D. J. Franzbach, J. Koruza, A. Benčan, B. Malič, M. Kosec, J. L. Jones, and K. G. Webber, Phys. Rev. B **87**, 094116 (2013).
[21]A. Snigirev, I. Snigireva, G. Vaughan, J. Wright, M. Rossat, A. Bytchkov, and C. Curfs, J. Phys.: Conf. Ser. **186**, 012073 (2009).
[22]P. Coan, A. Peterzol, S. Fiedler, C. Ponchut, J. C. Labiche, and A. Bravin, J. Synchrotron Radiat. **13**, 260–270 (2006).
[23]J. C. Labiche, O. Mathon, S. Pascarelli, M. A. Newton, G. G. Ferre, C. Curfs, G. Vaughan, A. Homs, and D. F. Carreiras, Rev. Sci. Instrum. **78**, 091301 (2007).
[24]See http://admet.com/products/universal-testing-machines/ for a description of the loading device.
[25]J. D. Almer and R. A. Winholtz, "X-ray stress analysis," in *Handbook of Experimental Solid Mechanics*, edited by W. N. Sharpe (Springer, 2008).
[26]L. Daniel, D. A. Hall, and P. J. Withers, Mech. Mater. **71**, 85–100 (2014).
[27]J. E. Huber, N. A. Fleck, C. M. Landis, and R. M. McMeeking, J. Mech. Phys. Solids **47**, 1663 (1999).
[28]M. Kamlah, A. C. Liskowsky, R. M. McMeeking, and H. Balke, Int. J. Solids Struct. **42**, 2949 (2005).
[29]L. Daniel, D. A. Hall, and P. J. Withers, "A multiscale modelling analysis of the contribution of crystalline elastic anisotropy to intergranular stresses in ferroelectric materials," J. Phys. D: Appl. Phys. (submitted).
[30]M. Bornert, T. Bretheau, and P. Gilormini, *Homogénéisation en mécanique des matériaux. Tome 1: Matériaux aléatoires élastiques et milieux périodiques* (Hermès Science, 2001).
[31]M. Bornert, T. Bretheau, and P. Gilormini, *Homogénéisation en mécanique des matériaux. Tome 2: Comportements non linaires et problèmes ouverts* (Hermès Science, 2001).
[32]R. Corcolle, L. Daniel, and F. Bouillault, Phys. Rev. B **78**(21), 214110 (2008).
[33]J. D. Eshelby, Proc. R. Soc. London, Ser. A **241**, 376–396 (1957).
[34]T. Mura, *Micromechanics of Defects in Solids* (Martinus Nijhoff Publishers, 1982).
[35]A. Sihvola, *Electromagnetic Mixing Formulas and Applications*, IEE Electromagnetic Waves Series, Vol. 47 (IET, 1999).
[36]G. W. Milton, *The Theory of Composites* (Cambridge University Press, 2002).